

High-pressure investigations in $\text{CH}_3\text{NH}_3\text{PbX}_3$ ($X = \text{I, Br, and Cl}$): Suppression of ion migration and stabilization of low-temperature structure

Yuk Tai Chan ^{1,*} Natanja Elliger ¹ Berina Klis,¹ Márton Kollár,² Endre Horváth,² László Forró ²,
Martin Dressel ^{1,†} and Ece Uykur^{1,3}

¹*Physikalisches Institut, Universität Stuttgart, D-70569 Stuttgart, Germany*

²*Laboratory of Physics of Condensed Matter, Institute of Physics,*

École Polytechnique Fédérale de Lausanne, CH-1015 Lausanne, Switzerland

³*Institute of Ion Beam Physics and Materials Research, Helmholtz-Zentrum Dresden-Rossendorf, D-01328 Dresden, Germany*



(Received 16 August 2022; accepted 1 December 2022; published 12 December 2022)

Hybrid organic-inorganic halide perovskites represent a promising next-generation photovoltaic material with drawbacks for structure stability and composition concerns. Demonstrations of ion migration and molecular dynamics suggest room for structural contraction and subsequent property adjustments. Here, we deploy dielectric and infrared spectroscopy under external pressure to probe the full structural phase diagram and dielectric response of methylammonium lead halide perovskites $\text{CH}_3\text{NH}_3\text{PbX}_3$ ($X = \text{I, Br, or Cl}$). Ion migration can be fully suppressed by pressure beyond 4 GPa. The low-temperature orthorhombic phase transition can be gradually enhanced and stabilized at ambient conditions with increasing pressure. A slow relaxation mode, presumably the motion of the CH_3NH_3^+ cation, is observed at lower pressure and is absent in the orthorhombic phase for every halide.

DOI: [10.1103/PhysRevB.106.214106](https://doi.org/10.1103/PhysRevB.106.214106)

I. INTRODUCTION

Hybrid organic-inorganic methylammonium lead halide perovskites $\text{CH}_3\text{NH}_3\text{PbX}_3$ ($X = \text{I, Br, or Cl}$), hereafter abbreviated as MAPX, have incentivized intense research efforts owing to their promising photovoltaic and optoelectronic applications [1–5]. Solar cells made with MAPX exhibit high power-conversion efficiency with low fabrication cost and offer composition variations for the adjustment of optoelectronic properties and multijunction design [6]. The downside is a short lifespan due to low stability and potential environmental hazard due to lead usage [7–9].

This naturally triggered the search for more suitable materials with similar spectacular properties; however, this turned out not to be a straightforward task due to the lack of understanding of the fundamental physical properties behind these materials. For instance, the effect of excitons on the observed behavior, the role of spin-orbit coupling, and defect formation and ion migration remain controversial [10–13]. As the lattice dynamics directly influences the electronic properties, understanding lattice dynamics in these compounds is of utmost importance.

External pressure, in this regard, is a suitable tuning parameter, as it allows one to gradually change the underlying structure. Indeed, many pressurization experiments have been conducted to study the evolution of structures and electronic properties of MAPX. However, due to the dynamic nature of the observed changes, reports on the high-pressure phases

have been controversial. There seems to be general consensus that due to the soft nature of MAPX, a series of structural phase transitions occurs [5,14–18]. At highest pressure, amorphization of the crystals was often claimed [15,16,19–23], but it has been challenged by its abnormal reversibility and persistent Bragg reflections and Raman features [19,24–26].

In addition to the crystal structure, research efforts have been invested in the ion dynamics and ion migration in MAPX crystals. Ion migration has been demonstrated to be a substantial factor for photovoltaic properties and structural stability at room temperature and ambient pressure in MAPbI_3 through measurements and computational studies [13,27–30]. Ion migration also leads to a gigantic dielectric permittivity at the DC limit [31–35] because of stoichiometric polarization, i.e., accumulation of propagating ions blocked at the interfaces between electrical contacts and solid surfaces. Previous studies gave strong evidence that the dominating mobile ion in the I compound is the halide unit, I^- [36,37]. Nonetheless, other ions like MA^+ or even Pb^{2+} and H^+ are eligible to perform migration [36–40], such that the observed response is a collection of all the contributions. Given a large X^- and MA^+ ion migration, the decomposition of PbX_3 into PbX_2 is proposed as a source of degradation [30,41].

Molecular motions of ions, particularly of MA^+ , also affect the light-harvesting efficiency. Photoinduced electron recombination time is prolonged if the electron is aligned and coupled with the neighboring MA^+ , so a fast MA^+ motion is favorable for the carrier lifetime [42–44]. The MA^+ ion is not strictly confined within the inorganic PbX_3^- octahedra framework at ambient conditions as rotation around the C-N axis, wobbling, and jumplike reorientation of MA^+ within the

*yuk-tai.chan@pi1.uni-stuttgart.de

†dressel@pi1.physik.uni-stuttgart.de

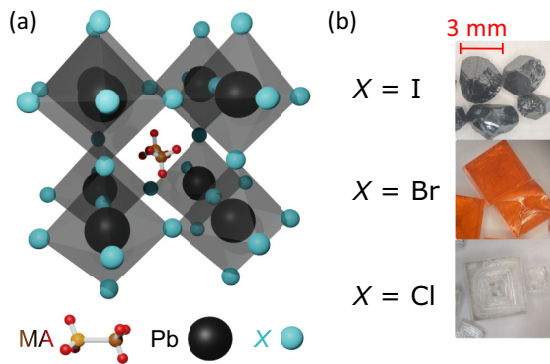


FIG. 1. (a) Crystal structure of MAPX at ambient pressure and high temperature, i.e., the cubic phase. (b) Photographs of the MAPX ($X = \text{I, Br, and Cl}$) single crystals. The bromide and chloride are in the cubic phase at ambient conditions, so the crystals are rectangular, whereas the iodide is in the tetragonal phase. For pressure measurements, 100 μm size shards from the 3 mm big crystals were used.

cage and transition between cages are all allowed [45–47]. For example, structural modulation under pressure is proven to have an impact on the carrier lifetime [48]. In addition, the substitution of a halide ion will also vary the MA^+ dynamics [30,49].

We employed dielectric and infrared spectroscopy under pressure to track the evolution of the structure, dielectric permittivity, and AC conductivity of MAPX. A completed structural phase diagram beyond the stabilization of the low-temperature orthorhombic phase to room temperature is probed for all halides. Ion migration is found to be gradually suppressed by pressure. Before the transition into the orthorhombic phase, a dielectric relaxation appears and is believed to be the translation motion of the MA^+ ion within or between the PbI_3^- cages because of its long relaxation time. With these, the low-temperature phases are bridged by the room temperature, high-pressure phases, and a complete picture of the structural transitions and their relation to the conduction properties is provided.

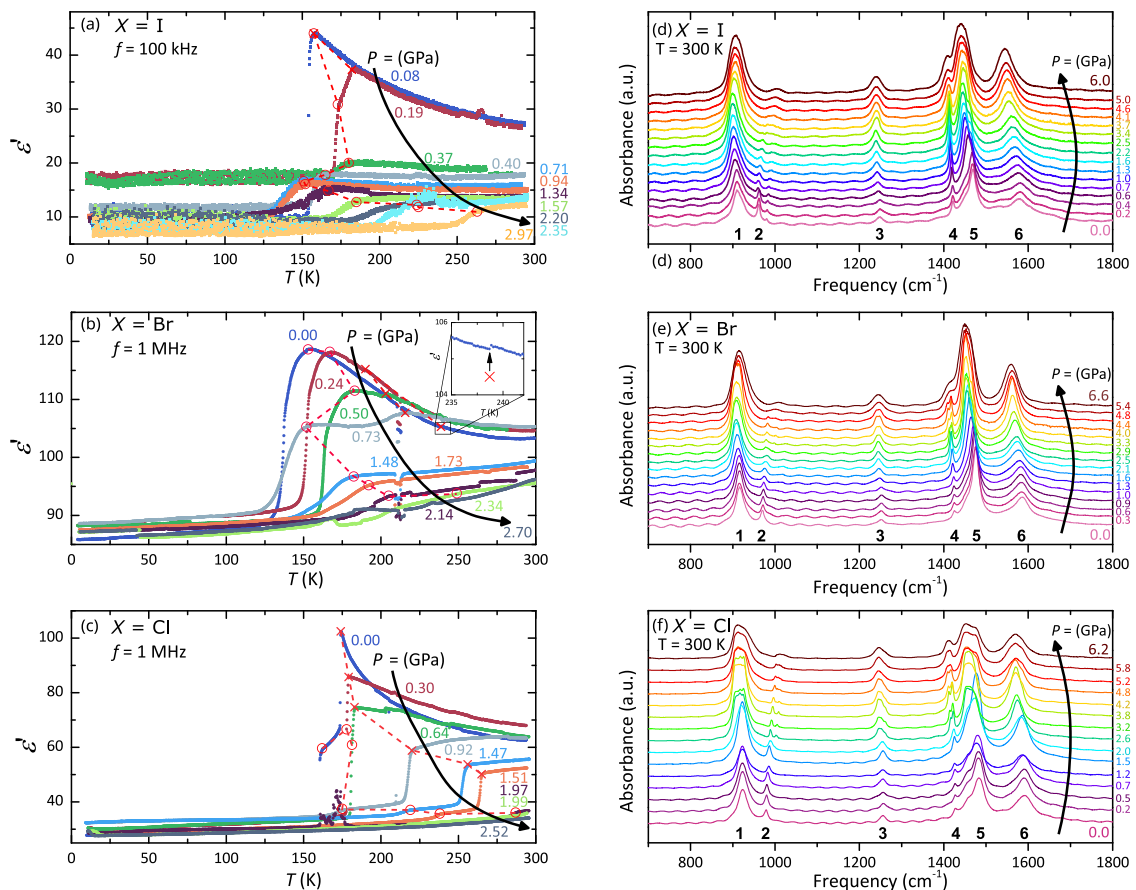


FIG. 2. (a)–(c) The temperature dependence of the real dielectric permittivity ϵ' under pressure in MAPX with $X = \text{I, Br, and Cl}$, respectively. Structural transitions are indicated by sudden changes in the magnitude of ϵ' . The transition temperature is marked as the beginning of the drop and is denoted by two symbols, \times and \circ . The transitions represented by the symbols are different between low and high pressure (see Fig. 3). Red dashed lines are guides for the eye to track the changes in transition temperatures. The transition temperature is shifted, and the width of the transition is progressively broadened as pressure rises. A waterfall version of these plots can be found in the Supplemental Material [51]. (d)–(f) Pressure-dependent absorption spectra at room temperature in MAPX with $X = \text{I, Br, and Cl}$, respectively. Six vibration modes of the methylammonium cation can be identified in the spectra. Other small features originated from Fabry-Pérot resonance. Structural transitions are reflected by shifting, broadening, and splitting of the vibration modes. The moment of transition is illustrated more clearly in the pressure evolution of the mode position [see Figs. 3(a)–3(c)].

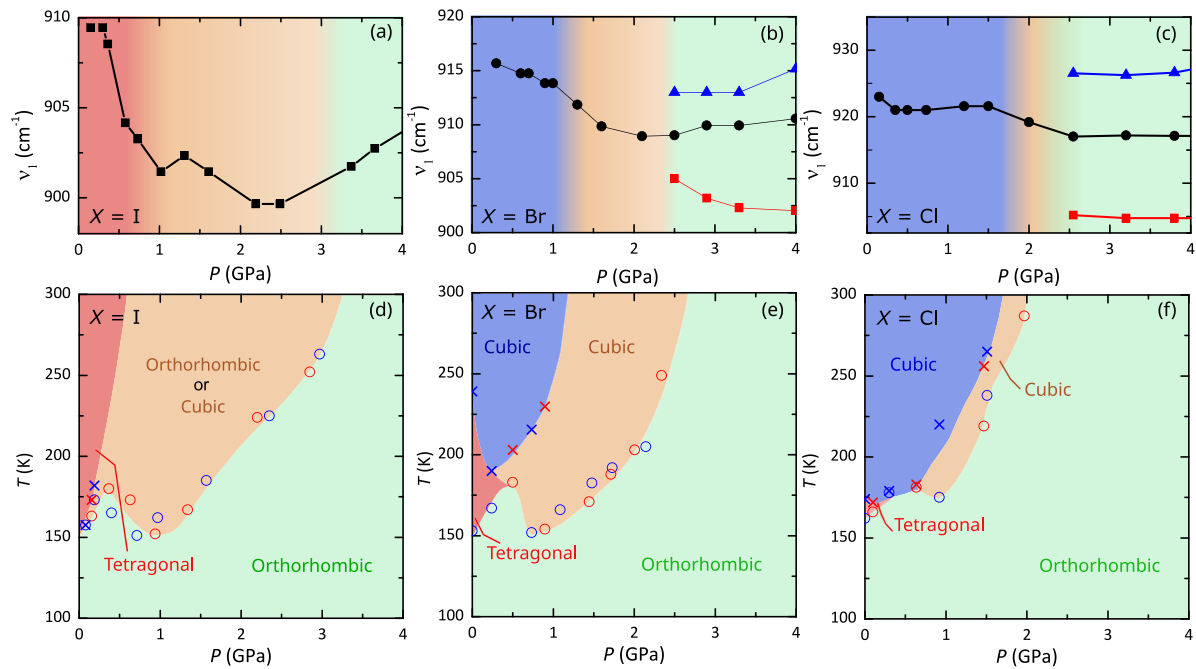


FIG. 3. (a)–(c) The pressure evolution of vibration mode 1 in the IR spectra of MAPX at room temperature with $X = \text{I}$, Br , and Cl , respectively. Crystal system transition (cubic-to-tetragonal or tetragonal-to-orthorhombic) is pointed out by the splitting of the mode or a large change in slope/trend, whereas the isostructural transition is inferred from a mild change in slope/trend. The pressure evolutions of two other vibration modes in each of the MAPX are plotted in Fig. S3 in the Supplemental Material [51]. (d)–(f) The T - P phase diagrams of MAPX with $X = \text{I}$, Br , and Cl , respectively. Blue and red markers in the phase diagrams represent cooling and warming processes. The structure (cubic, tetragonal, or orthorhombic) is inferred by incorporating the dielectric data, IR vibration mode evolutions, and structural analysis from the literature [14–16,19,20,24,52,54,55]. The low-temperature orthorhombic phase is stabilized to room temperature at about 3.2, 2.6, and 2 GPa for $X = \text{I}$, Br , and Cl , respectively.

II. EXPERIMENTAL DETAILS

High-quality single crystals of $\text{CH}_3\text{NH}_3\text{PbX}_3$ [$X = \text{I}$, Br , Cl ; Fig. 1(b)] were synthesized by solution growth as documented elsewhere [50]. The radio-frequency dielectric measurements from 1 Hz to 1 MHz were performed using an autobalance bridge (Agilent 4294A) and a frequency-response analyzer (Novocontrol Alpha Analyzer) with the standard quasi-four-probe technique. The electrical contacts were made with silver paste 3303B and gold wires. The applied measuring alternating voltage was set to 1 V, which was tested to check that it remained in the linear regime. Low-temperature environment was provided by a custom-made helium-flow cryostat, and the base temperature reached was 4 K. The cooling and heating rates were 2 K min^{-1} . Infrared (IR) transmission spectra between 600 and 8000 cm^{-1} were measured using the Bruker VERTEX 80v FTIR spectrometer. Since the reflectivity of the samples is negligible, the absorbance A was converted via the Lambert-Beer law, $A = -\ln \text{Tr}(\omega)$, where $\text{Tr}(\omega)$ is the transmittance. The vibration modes were modeled with Lorentzians.

The high-pressure environment was achieved with screw-driven diamond anvil cells (Almax EasyLab). For the dielectric measurements, the anvils had a $600 \mu\text{m}$ culet diameter. A $250 \mu\text{m}$ diameter hole at the center of a copper beryllium gasket was used as a cavity for sample insertion. Daphne oil 7474 was used as the pressure transmitting medium for hydrostaticity. The pressure determination was done by ruby fluorescence spectroscopy at room temperature.

The ruby fluorescence spectra from each pressure cell of MAPX in dielectric measurements are plotted in the Appendix (Fig. 6). The highest pressure reached was 5.93 GPa. For the IR measurements, the anvils' culets were $800 \mu\text{m}$ in diameter, and the sample cavity was $250 \mu\text{m}$ in diameter. The pressure transmitting medium was CsI powder. Like in the dielectric measurements, ruby fluorescence spectroscopy at room temperature was the method of pressure determination. The highest pressure reached was 6.6 GPa.

III. RESULTS AND DISCUSSION

Figures 2(a)–2(c) depict the temperature dependence of the real dielectric permittivity ϵ' of MAPX at various pressures. An exact determination of the geometrical factors in a diamond anvil cell is a challenging task. Therefore, the absolute values of the converted physical properties, e.g., ϵ' , cannot be determined precisely. However, a quick comparison of the lowest pressure values with the ambient pressure literature values [14,33,34,52] suggests that the permittivities presented in this study reasonably agree with the literature. A slight change in the geometrical factors with increasing pressure is also seen; however, the temperature dependence of the dielectric permittivity should remain valid.

The structural transition in MAPX is reflected by the sudden drop in ϵ' . Progressively, the characteristic drop in ϵ' of the structural transition broadens as domains are formed among the crystal and their transitions stagger, so the transition temperature here is defined by the start of the drop.

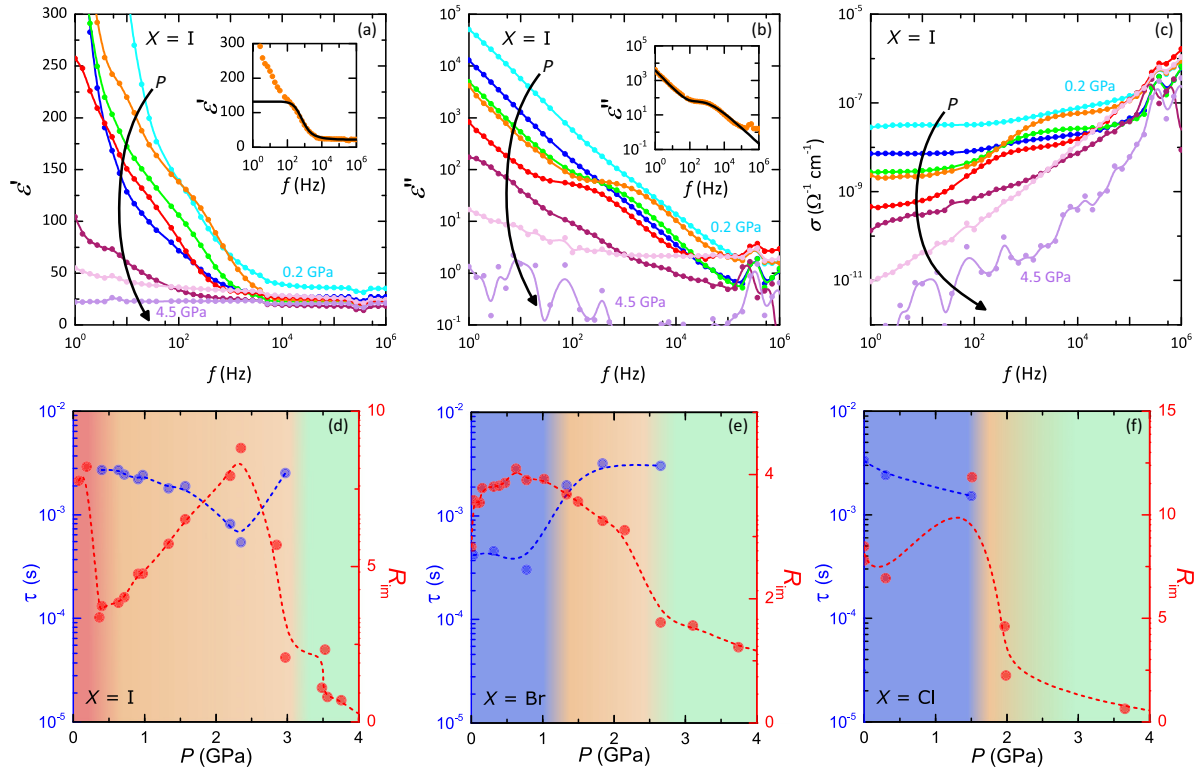


FIG. 4. (a)–(c) Frequency dependence of the dielectric properties of MAPbI₃ at room temperature under pressure (those with $X = \text{Br}$ and Cl are given in the Appendix). (a) $\epsilon'(f)$: The stoichiometric polarization is observed at low pressures and is gradually suppressed as pressure increases. This vanishing of polarization indicates the localization of the migrating ions. Inset: The fitting result of Eq. (1) for $\epsilon'(f)$ at 2.4 GPa. (b) $\epsilon''(f)$: The linear relation due to ionic conduction is identified at low frequency and at low pressure, which similarly vanishes as pressure rises. A dielectric relaxation is observed, on top of the linear background due to ionic conduction, around $f = 1$ kHz at certain pressure points. Inset: the fitting result of Eq. (1) for $\epsilon''(f)$ at 2.4 GPa. (c) $\sigma(f)$: The magnitude of $\sigma(f)$ at low frequencies is reduced by pressure and drops below the magnitude of ionic conductivity at ambient pressure, indicating the localization of ions. (d)–(f) Pressure dependence of the relaxation time τ and the stoichiometric polarization ratio R_{im} for $X = \text{I}$, Br , and Cl , respectively. τ is absent, and R_{im} dies out beyond P^* , indicating the prohibition of an ionic motion and a full suppression of the ion migration in the orthorhombic phase.

Two transitions can be observed in $X = \text{Br}$ and Cl which are denoted with \times and \circ symbols, but the transition represented by the same symbols changes between low and high pressures (see Fig. 3). In all halides, the orthorhombic transition temperature is gradually enhanced, and the size of the drop is suppressed by pressure.

Figures 2(d)–2(f) show the infrared absorbance spectra of MAPX at room temperature at various pressures. Six vibration modes of the methylammonium cation are identified in the spectra. After cross-referencing with Ref. [53], the six modes correspond to (1) CH₃ rocking, (2) C-N stretching, (3) NH₃ rocking, (4) symmetric CH₃ bending, (5) symmetric NH₃ bending, and (6) asymmetric NH₃ bending. The shoulder in mode 5 at around 1455 cm⁻¹ corresponds to asymmetric CH₃ bending. The other small features originate from Fabry-Pérot resonance. The vibration modes exhibit shifting, broadening, and splitting under pressure and when undergoing transitions. The moment of transition is illustrated more clearly in the pressure evolution of the mode position. Figures 3(a)–3(c) show the evolution of vibration mode 1 under pressure. Crystal system transition is pointed out by the splitting of the mode or a large change in slope or trend, whereas the isostructural transition is inferred from a mild change. The pressure

evolution of the other modes is given in the Supplemental Material [51].

Figures 3(d)–3(f) depict the T - P phase diagrams of all halides resolved by incorporating the dielectric data, room temperature IR measurement results, and the structural analysis from the literature [14–16, 19, 20, 24, 52, 54, 55]. The low-pressure phase diagrams are in agreement with the pioneer study by Gesi [14] in which the pressure ceiling is 0.7 GPa. By extending the pressure range up to 4 GPa, we observed the reappearance of an intermediate phase between the cubic and orthorhombic phases in $X = \text{Cl}$, and the stabilization of the low-temperature orthorhombic structural phase to room temperature occurred in every halide compound. The stabilization pressure P^* is about 3.2, 2.6, and 2 GPa for $X = \text{I}$, Br , and Cl , respectively.

Changing from $X = \text{I}$ to Cl , the phase diagram reveals that the high-temperature cubic phase (indicated in blue) and the low-temperature orthorhombic phase (indicated in green) get closer, while the intermediate region is divided into two phases and the point of separation is indicated by the peak of the dome in the orthorhombic phase. P^* decreases from 3.2 to 2 GPa, such that the adaptation of smaller halide ions is in favor of the formation of a homogeneous lattice.

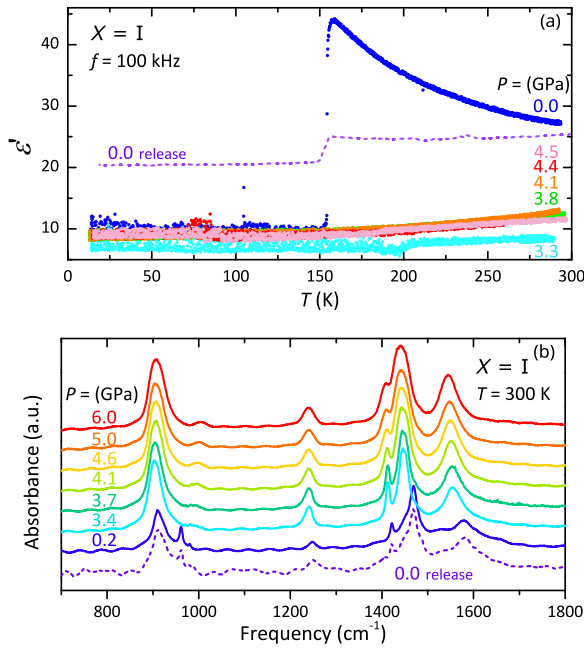


FIG. 5. High-pressure (a) dielectric permittivity $\epsilon'(T)$ and (b) IR absorption spectra of MAPbI₃ at pressure above their P^* . The pressure range reaches above 4.5 GPa and is well above the literature amorphization pressure. No prominent anomaly is noticed in ϵ' . Broadening of the resonance peak occurs in IR spectra, but the peaks remain pronounced and totally identifiable. Upon pressure release, both the sharp transition in $\epsilon'(T)$ and resonance peaks in IR spectra are restored.

The frequency dependences of the real dielectric permittivity ϵ' , imaginary dielectric permittivity ϵ'' , and AC conductivity σ under pressure for MAPbI₃ are plotted in Figs. 4(a)–4(c). At ambient pressure, ϵ' shows an increase towards low frequencies as a signature of the stoichiometric polarization [31]. With increasing pressure, it is gradually suppressed and eventually disappears at sufficiently high pressures. The degree of the stoichiometric polarization is quantified by calculating the ratio of ϵ' between low and high frequencies, $R_{\text{im}} = [\epsilon'(10 \text{ Hz}) - \epsilon'(1 \text{ MHz})]/\epsilon'(1 \text{ MHz})$. Similarly, for ϵ'' , an f^{-1} relation due to conduction is seen at low pressures and dies out as pressure rises. On the other hand, the AC conductivity σ is also greatly suppressed by pressure and drops more than 2 orders of magnitude above 2 GPa. Qualitatively similar behavior was also observed for $X = \text{Br}$ and Cl , and the details are given in the Appendix (Fig. 7).

These observations can be concurrently explained by the localization of the ionic charges under pressure. Electronic and ionic conductivities in MAPbI₃ are both of the order of 1 nS cm^{-1} at ambient conditions [31]. Under pressure, the macroscopic conductivity drops below 1 nS cm^{-1} ; necessarily, both conduction are reduced by pressure, presumably due to the enhanced electrostatic confinement accompanied by the decrease of the lattice constants. Because of the ion localization, both the ionic conduction and stoichiometric polarization are reduced, resulting in the flattening of the gigantic increase in ϵ' at low frequencies as $f \rightarrow 0$ and the reduction of the linear background in ϵ'' spectra.

Besides the migrating X^- ions, the MA^+ cation also shows signs of freedom reduction under pressure. A paraelectric Curie-Weiss behavior that occurs in $\epsilon'(T)$ at high temperature at ambient pressure is found to be gradually suppressed by pressure [Figs. 2(a)–2(c)]. The paraelectric behavior entails the tendency of alignment of MA^+ dipoles with the external field and indicates that the MA^+ cation is not restricted from reorientation by the environment in the lattice. The disappearance of paraelectric behavior takes place at pressure points that coincide with the early structural transitions, identified in IR spectra, at $P_{\text{div}} = 0.6, 1.0,$ and 1.5 GPa for $X = \text{I}, \text{Br},$ and Cl , respectively. This feature points to a reduction of freedom for the MA^+ cation accompanied by the structural transition, and the hydrogen bonding between the MA^+ cation and the PbX_6 tetrahedral network is held responsible.

Above P_{div} , the magnitude of ϵ' drops with pressure. Since the polar MA^+ ion is rigid, the contraction of the C-N bond is unlikely to happen. This suppression of the polarization is thus attributed as the cause of the further diminishment of MA^+ rotation and the reduction of delocalized ions and electrons at high pressures.

An unreported relaxation is observed in every halide at pressures prior to P^* . The dielectric relaxation is primarily described by the Havriliak-Negami equation [56]:

$$\epsilon^* = \epsilon_\infty + \frac{\epsilon_s - \epsilon_\infty}{[1 + (i\omega\tau)^{1-\alpha}]^\beta}, \quad (1)$$

where ϵ_s and ϵ_∞ are the static permittivity and permittivity at the high-frequency limit, τ is the relaxation time, and α and β are empirical control parameters for symmetric and asymmetric broadening. The relaxation time τ is found to be about 1 ms. Because of the slow τ , this relaxation will not be the translational migration of X^- ions or the rotation, reorientation, or vibrations of MA^+ . Diffusion of Pb^{2+} is unlikely because of its larger mass and charges [36,57]; meanwhile, the MA^+ cation is suggested for slower migration [58,59]. Therefore, this relaxation at kilohertz is most likely to be the translation motion of MA^+ within or between cages [45–47].

Figures 4(d)–4(f) depict the pressure dependence of the relaxation time τ and R_{im} to illustrate the correlation between the ion motions and the structural phases. The relaxation behaves similarly among different halides, with some deviations such as the trend within one structural phase and the abrupt jumps across structures. In all cases, the relaxation is fully prohibited in the high-pressure orthorhombic phase. This observation of dielectric relaxation aligns with the picture of reduced translational and rotational disorders of MA^+ ions from the tetragonal/cubic to orthorhombic phase [25,33,54,60,61]. R_{im} represents the extent of ion migration, and it exhibits changes across structural transitions. Similar to τ , a full prohibition occurs on R_{im} after transformation into the orthorhombic phase, indicating a full negation of ion migration, such that ion migration and the MA^+ cation's translational and rotational motions are all greatly suppressed in the most anisotropic orthorhombic phase, with only the thermally excited small-amplitude rotation of ions remaining.

The dielectric permittivity $\epsilon'(T)$ and IR absorption spectra of MAPbI₃ at a higher pressure range are shown in Fig. 5, whereas those for $X = \text{Br}$ and Cl are in the Appendix (Fig. 8). All halides are pressurized well above the literature

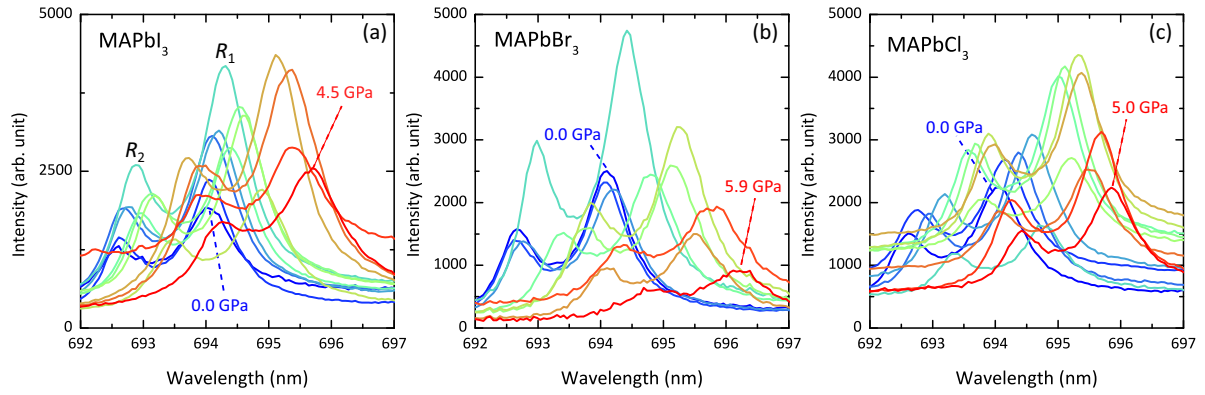


FIG. 6. The ruby fluorescence spectra of each pressure cell for MAPX with $X =$ (a) I, (b) Br, and (c) Cl. The pressure inside the pressurized cavity is measured by the R_1 peak position (the peak located at the longer wavelength) using Eq. (A1).

amorphization pressures (about 3, 2.7, and 2.4 GPa for $X =$ I, Br, and Cl, respectively). For all of them, no anomaly is noticeable from $\epsilon'(T)$ after the stabilization of the low-temperature structural phase. Similarly, in the IR spectra, although broadening occurs, the vibration resonance peaks remain discernible. Upon pressure release, both signatures of the uniform lattice structure, the sharp drop in ϵ' and the pronounced vibration resonance peak in IR absorption spectra, are restored, which is abnormal if the crystal has undergone amorphization. Given the ambiguity of the amorphous state and the coincidence of the low-temperature structural phase

stabilization pressure P^* with the literature amorphization pressures, it is plausible to suggest that the amorphous state observed in the literature is, instead of a fully disordered random lattice, the orthorhombic phase with pressure-induced distortions.

Significant growth in the magnitude of ϵ' is observed for $X =$ Br and Cl. After pressure is released, part of the growth remains at ambient pressure (Fig. S3). This could be an artificial gain due to the enlargement of the electrical contacts' area. However, the chemically related perovskite candidate $\text{CH}_3\text{NH}_3\text{SnI}_3$ exhibits enhanced electrical conductivity and

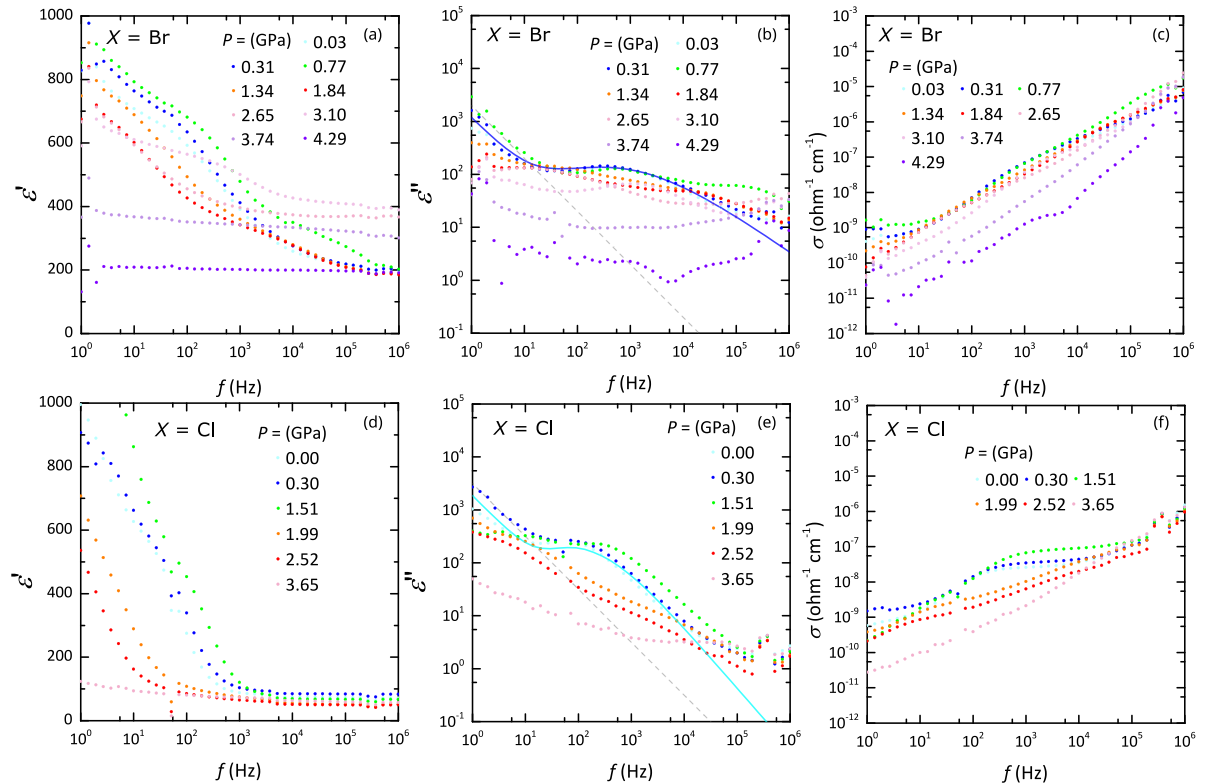


FIG. 7. Frequency dependence of the dielectric properties: real dielectric permittivity ϵ' , imaginary dielectric permittivity ϵ'' , and AC conductivity σ for (a)–(c) $X =$ Br and (d)–(f) $X =$ Cl. In accordance with those for $X =$ I, the stoichiometric polarization for ϵ' is progressively diminished as pressure increases and is fully negated at pressures above P^* . The conductivity drops below 1 nS cm^{-1} , implying the reduction of ionic conductivity by pressure. A relaxation is also captured and located at 1 kHz, which disappears beyond P^* .

structural stability following pressure treatment [62], so the growth in dielectric permittivity could potentially be an intrinsic property of $\text{CH}_3\text{NH}_3\text{PbX}_3$.

IV. CONCLUSION

In summary, the structural phase diagrams of $\text{CH}_3\text{NH}_3\text{PbX}_3$ ($X = \text{I}, \text{Br}, \text{and Cl}$) well above the indeterminate amorphization pressure have been investigated. For all halides, the low-temperature orthorhombic phase is stabilized up to room temperature at $P^* = 3.2, 2.6,$ and 2 GPa for $X = \text{I}, \text{Br},$ and Cl , respectively. Ion migration in $\text{CH}_3\text{NH}_3\text{PbX}_3$ can be effectively suppressed by pressure, as evidenced by the gradual suppression of stoichiometric polarization and conductivity of $\text{CH}_3\text{NH}_3\text{PbX}_3$ under pressure. A dielectric relaxation mode is observed in the cubic or tetragonal phases of $\text{CH}_3\text{NH}_3\text{PbX}_3$ and is consistently absent in the orthorhombic phase. This relaxation is likely to be the translational motion of MA^+ because of its slow timescale, which implies the localization of MA^+ in the orthorhombic phase. Finally, no anomaly is observed in dielectric permittivity spectra at or beyond the reported amorphization pressure. Because of the reversibility and coincidence of P^* with the amorphization pressures, the observed amorphization in $\text{CH}_3\text{NH}_3\text{PbX}_3$ is hypothesized to be the orthorhombic phase with inhomogeneous distortions.

ACKNOWLEDGMENTS

We thank G. Untereiner for her technical support. E.U. acknowledges the European Social Fund and the Baden-Württemberg Stiftung for the financial support for this research project by the Eliteprogramme.

APPENDIX

1. Pressure determination: Ruby fluorescence

The ruby fluorescence spectra from each pressure cell of MAPX in dielectric measurements are plotted in Fig. 6. The relationship between pressure and the fluorescence R_1 peak is given by

$$P(\lambda) = \frac{1904}{7.665} \left[\left(\frac{\lambda}{\lambda_a} \right)^{7.665} - 1 \right], \quad (\text{A1})$$

where the calibration by Mao *et al.* [63] is used and λ_a is the R_1 peak position at ambient pressure. The fluorescence peak positions shift linearly with pressure. The width of the peaks also increases with pressure, which is the result of the inhomogeneous pressure distribution in the cavity.

2. Frequency dependence of dielectric properties of $X = \text{Br}, \text{Cl}$

The frequency dependences of the physical properties ϵ' , ϵ'' , and σ for $X = \text{Br}$ and $X = \text{Cl}$ are displayed in Figs. 7(a)–7(c) and 7(d)–7(f), respectively. Like for $X = \text{I}$, suppression of the low-frequency stoichiometric polarization is observed at high pressure in both $X = \text{Br}$ and Cl . The magnitude of σ for both $X = \text{Br}$ and Cl drops by two orders and is below 1 nS cm^{-1} , so the reduction of the ionic conduction also takes place in these halides. From the ϵ'' spectra, a relaxation peak

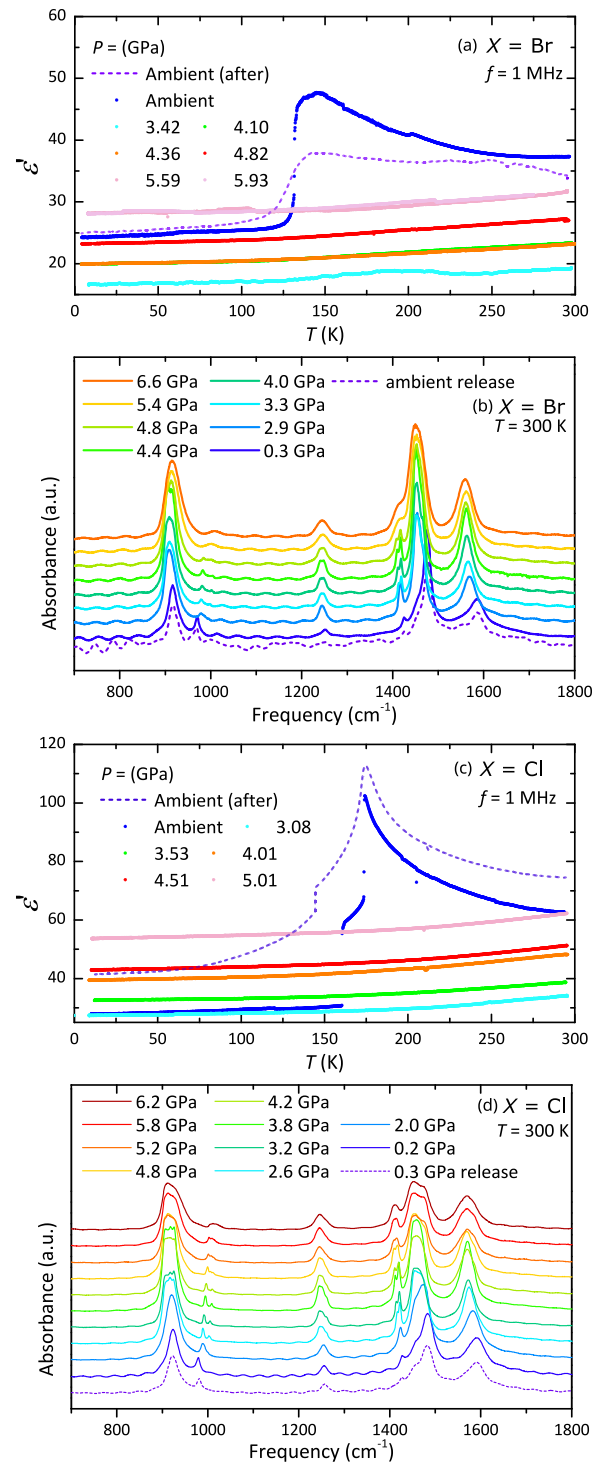


FIG. 8. High-pressure dielectric permittivity $\epsilon'(T)$ and IR absorption spectra of (a) and (b) MAPB and (c) and (d) MAPC at pressures above their P^* . The pressure range has reached above 4.5 GPa and is well above the literature amorphization pressure. No prominent anomaly is noticed in ϵ' . Broadening of the resonance peak occurs in IR spectra, but the peaks remain pronounced and totally identifiable. Upon pressure release, both the sharp drop in $\epsilon'(T)$ and resonance peaks in IR spectra are restored. This is clearly identified at low pressure in both halides. Upon pressure application, besides the decay of the $1/f$ background due to conduction, the relaxation peak disappears suddenly at pressure, coinciding with the orthorhombic phase transition.

3. High pressures above P^* and upon release

Figure 8 depicts the dielectric permittivity $\epsilon'(T)$ and IR spectra for $X = \text{Br}$ and Cl . In both halides, above P^* , no prominent feature develops, but growth in magnitude occurs. Upon pressure release, for $X = \text{Br}$, the size of the paraelectric divergence at higher temperatures in the tetragonal phase is significantly reduced. Other than that, the transition temperature and low-temperature magnitude of polarization behave the same as before the pressure cycle, so the growth of ϵ' under high pressure might be an intrinsic feature for

$X = \text{Br}$. However, for $X = \text{Cl}$, the growth in ϵ' at high pressure remains after pressure is removed, so this gain in ϵ' is seemingly pressure irrelevant. Nonetheless, the landscape of the structural transition has been modified a bit, but its temperature is restored after the pressure cycle. In the IR spectra, the signature resonance peaks remain totally discernible with only mild broadening until the high pressure of 6 GPa, and the sharp peaks mostly recover after pressure is lifted. These two observations imply that no destructive amorphization happens at high pressure, and the lattice structure is mostly restored, with some minor distortion remaining after the pressure cycle.

-
- [1] A. Kojima, K. Teshima, Y. Shirai, and T. Miyasaka, Organometal halide perovskites as visible-light sensitizers for photovoltaic cells, *J. Am. Chem. Soc.* **131**, 6050 (2009).
- [2] M. A. Green, A. Ho-Baillie, and H. J. Snaith, The emergence of perovskite solar cells, *Nat. Photonics* **8**, 506 (2014).
- [3] Q. Jiang, Z. Chu, P. Wang, X. Yang, H. Liu, Y. Wang, Z. Yin, J. Wu, X. Zhang, and J. You, Planar-structure perovskite solar cells with efficiency beyond 21%, *Adv. Materials* **29**, 1703852 (2017).
- [4] X. Lü, W. Yang, Q. Jia, and H. Xu, Pressure-induced dramatic changes in organic-inorganic halide perovskites, *Chem. Sci.* **8**, 6764 (2017).
- [5] M. Li, T. Liu, Y. Wang, W. Yang, and X. Lü, Pressure responses of halide perovskites with various compositions, dimensionalities, and morphologies, *Matter Radiat. Extremes* **5**, 018201 (2020).
- [6] W.-J. Yin, T. Shi, and Y. Yan, Unusual defect physics in $\text{CH}_3\text{NH}_3\text{PbI}_3$ perovskite solar cell absorber, *Appl. Phys. Lett.* **104**, 063903 (2014).
- [7] T. Leijtens, G. E. Eperon, N. K. Noel, S. N. Habisreutinger, A. Petrozza, and H. J. Snaith, Stability of metal halide perovskite solar cells, *Adv. Energy Mater.* **5**, 1500963 (2015).
- [8] T. A. Berhe, W.-N. Su, C.-H. Chen, C.-J. Pan, J.-H. Cheng, H.-M. Chen, M.-C. Tsai, L.-Y. Chen, A. A. Dubale, and B.-J. Hwang, Organometal halide perovskite solar cells: Degradation and stability, *Energy Environ. Sci.* **9**, 323 (2016).
- [9] B. Saparov and D. B. Mitzi, Organic-inorganic perovskites: Structural versatility for functional materials design, *Chem. Rev.* **116**, 4558 (2016).
- [10] J. S. Manser and P. V. Kamat, Band filling with free charge carriers in organometal halide perovskites, *Nat. Photonics* **8**, 737 (2014).
- [11] J. Even, L. Pedesseau, J.-M. Jancu, and C. Katan, Importance of spin-orbit coupling in hybrid organic/inorganic perovskites for photovoltaic applications, *J. Phys. Chem. Lett.* **4**, 2999 (2013).
- [12] M. Saba, F. Quochi, A. Mura, and G. Bongiovanni, Excited state properties of hybrid perovskites, *Acc. Chem. Res.* **49**, 166 (2016).
- [13] Y. Yuan and J. Huang, Ion migration in organometal trihalide perovskite and its impact on photovoltaic efficiency and stability, *Acc. Chem. Res.* **49**, 286 (2016).
- [14] K. Gesi, Effect of hydrostatic pressure on the structural phase transitions in $\text{CH}_3\text{NH}_3\text{PbI}_3$ ($X = \text{Cl}, \text{Br}, \text{I}$), *Ferroelectrics* **203**, 249 (1997).
- [15] I. P. Swainson, M. G. Tucker, D. J. Wilson, B. Winkler, and V. Milman, Pressure response of an organic-inorganic perovskite: Methylammonium lead bromide, *Chem. Mater.* **19**, 2401 (2007).
- [16] S. Jiang, Y. Fang, R. Li, H. Xiao, J. Crowley, C. Wang, T. J. White, W. A. Goddard, Z. Wang, T. Baikie, and J. Fang, Pressure-dependent polymorphism and band-gap tuning of methylammonium lead iodide perovskite, *Angew. Chem.* **128**, 6650 (2016).
- [17] T. Ou, J. Yan, C. Xiao, W. Shen, C. Liu, X. Liu, Y. Han, Y. Ma, and C. Gao, Visible light response, electrical transport, and amorphization in compressed organolead iodine perovskites, *Nanoscale* **8**, 11426 (2016).
- [18] M. Szafranski and A. Katrusiak, Photovoltaic hybrid perovskites under pressure, *J. Phys. Chem. Lett.* **8**, 2496 (2017).
- [19] Y. Wang, X. Lü, W. Yang, T. Wen, L. Yang, X. Ren, L. Wang, Z. Lin, and Y. Zhao, Pressure-induced phase transformation, reversible amorphization, and anomalous visible light response in organolead bromide perovskite, *J. Am. Chem. Soc.* **137**, 11144 (2015).
- [20] F. Capitani, C. Marini, S. Caramazza, P. Postorino, G. Garbarino, M. Hanfland, A. Pisanu, P. Quadrelli, and L. Malavasi, High-pressure behavior of methylammonium lead iodide (MAPbI_3) hybrid perovskite, *J. Appl. Phys.* **119**, 185901 (2016).
- [21] L. Kong, G. Liu, J. Gong, Q. Hu, R. D. Schaller, P. Dera, D. Zhang, Z. Liu, W. Yang, K. Zhu, Y. Tang, C. Wang, S.-H. Wei, T. Xu, and H. Kwang Mao, Simultaneous band-gap narrowing and carrier-lifetime prolongation of organic-inorganic trihalide perovskites, *Proc. Natl. Acad. Sci. USA* **113**, 8910 (2016).
- [22] L. Wang, K. Wang, G. Xiao, Q. Zeng, and B. Zou, Pressure-induced structural evolution and band gap shifts of organometal halide perovskite-based methylammonium lead chloride, *J. Phys. Chem. Lett.* **7**, 5273 (2016).
- [23] K.-H. Wang, L.-C. Li, M. Shellaiah, and K. W. Sun, Structural and photophysical properties of methylammonium lead tribromide (MAPbBr_3) single crystals, *Sci. Rep.* **7**, 13643 (2017).
- [24] A. Jaffe, Y. Lin, C. M. Beavers, J. Voss, W. L. Mao, and H. I. Karunadasa, High-pressure single-crystal structures of 3D lead-halide hybrid perovskites and pressure effects on their electronic and optical properties, *ACS Cent. Sci.* **2**, 201 (2016).
- [25] R. Zhang, W. Cai, T. Bi, N. Zarifi, T. Terpstra, C. Zhang, Z. V. Verdeny, E. Zurek, and S. Deemyad, Effects of nonhydrostatic stress on structural and optoelectronic properties of methylammonium lead bromide perovskite, *J. Phys. Chem. Lett.* **8**, 3457 (2017).

- [26] A. Francisco-López, B. Charles, O. J. Weber, M. I. Alonso, M. Garriga, M. Campoy-Quiles, M. T. Weller, and A. R. Goñi, Pressure-induced locking of methylammonium cations versus amorphization in hybrid lead iodide perovskites, *J. Phys. Chem. C* **122**, 22073 (2018).
- [27] J. M. Frost and A. Walsh, What is moving in hybrid halide perovskite solar cells?, *Acc. Chem. Res.* **49**, 528 (2016).
- [28] A. Dualeh, T. Moehl, N. Tétreault, J. Teuscher, P. Gao, M. K. Nazeeruddin, and M. Grätzel, Impedance spectroscopic analysis of lead iodide perovskite-sensitized solid-state solar cells, *ACS Nano* **8**, 362 (2014).
- [29] Z. Xiao, Y. Yuan, Y. Shao, Q. Wang, Q. Dong, C. Bi, P. Sharma, A. Gruverman, and J. Huang, Giant switchable photovoltaic effect in organometal trihalide perovskite devices, *Nat. Mater.* **14**, 193 (2015).
- [30] W. Tress, N. Marinova, T. Moehl, S. M. Zakeeruddin, M. K. Nazeeruddin, and M. Grätzel, Understanding the rate-dependent J - V hysteresis, slow time component, and aging in $\text{CH}_3\text{NH}_3\text{PbI}_3$ perovskite solar cells: The role of a compensated electric field, *Energy Environ. Sci.* **8**, 995 (2015).
- [31] T.-Y. Yang, G. Gregori, N. Pellet, M. Grätzel, and J. Maier, The significance of ion conduction in a hybrid organic-inorganic lead-iodide-based perovskite photosensitizer, *Angew. Chem., Int. Ed.* **54**, 7905 (2015).
- [32] J. G. Labram, D. H. Fabini, E. E. Perry, A. J. Lehner, H. Wang, A. M. Glaudell, G. Wu, H. Evans, D. Buck, R. Cotta, L. Echegoyen, F. Wudl, R. Seshadri, and M. L. Chabiny, Temperature-dependent polarization in field-effect transport and photovoltaic measurements of methylammonium lead iodide, *J. Phys. Chem. Lett.* **6**, 3565 (2015).
- [33] D. H. Fabini, T. Hogan, H. A. Evans, C. C. Stoumpos, M. G. Kanatzidis, and R. Seshadri, Dielectric and thermodynamic signatures of low-temperature glassy dynamics in the hybrid perovskites $\text{CH}_3\text{NH}_3\text{PbI}_3$ and $\text{HC}(\text{NH}_2)_2\text{PbI}_3$, *J. Phys. Chem. Lett.* **7**, 376 (2016).
- [34] I. Anusca, S. Balčiūnas, P. Gemeiner, Š. Svirskas, M. Sanjalp, G. Lackner, C. Fettkenhauer, J. Belovickis, V. Samulionis, M. Ivanov, B. Dkhil, J. Banyš, V. V. Shvartsman, and D. C. Lupascu, Dielectric response: Answer to many questions in the methylammonium lead halide solar cell absorbers, *Adv. Energy Mater.* **7**, 1700600 (2017).
- [35] W. Peng, C. Aranda, O. M. Bakr, G. Garcia-Belmonte, J. Bisquert, and A. Guerrero, Quantification of ionic diffusion in lead halide perovskite single crystals, *ACS Energy Lett.* **3**, 1477 (2018).
- [36] C. Eames, J. M. Frost, P. R. F. Barnes, B. C. O'Regan, A. Walsh, and M. S. Islam, Ionic transport in hybrid lead iodide perovskite solar cells, *Nat. Commun.* **6**, 7497 (2015).
- [37] J. M. Azpiroz, E. Mosconi, J. Bisquert, and F. D. Angelis, Defect migration in methylammonium lead iodide and its role in perovskite solar cell operation, *Energy Environ. Sci.* **8**, 2118 (2015).
- [38] R. Gottesman, E. Haltzi, L. Gouda, S. Tirosh, Y. Bouhadana, A. Zaban, E. Mosconi, and F. D. Angelis, Extremely slow photoconductivity response of $\text{CH}_3\text{NH}_3\text{PbI}_3$ perovskites suggesting structural changes under working conditions, *J. Phys. Chem. Lett.* **5**, 2662 (2014).
- [39] D. A. Egger, L. Kronik, and A. M. Rappe, Theory of hydrogen migration in organic-inorganic halide perovskites, *Angew. Chem., Int. Ed.* **54**, 12437 (2015).
- [40] Y. Yuan, J. Chae, Y. Shao, Q. Wang, Z. Xiao, A. Centrone, and J. Huang, Photovoltaic switching mechanism in lateral structure hybrid perovskite solar cells, *Adv. Energy Mater.* **5**, 1500615 (2015).
- [41] J. Zhao, Y. Deng, H. Wei, X. Zheng, Z. Yu, Y. Shao, J. E. Shield, and J. Huang, Strained hybrid perovskite thin films and their impact on the intrinsic stability of perovskite solar cells, *Sci. Adv.* **3**, eaao5616 (2017).
- [42] J. Gong, M. Yang, X. Ma, R. D. Schaller, G. Liu, L. Kong, Y. Yang, M. C. Beard, M. Lesslie, Y. Dai, B. Huang, K. Zhu, and T. Xu, Electron-rotor interaction in organic-inorganic lead iodide perovskites discovered by isotope effects, *J. Phys. Chem. Lett.* **7**, 2879 (2016).
- [43] D. J. Kubicki, D. Prochowicz, A. Hofstetter, P. Péchy, S. M. Zakeeruddin, M. Grätzel, and L. Emsley, Cation dynamics in mixed-cation $(\text{MA})_x(\text{FA})_{1-x}\text{PbI}_3$ hybrid perovskites from solid-state NMR, *J. Am. Chem. Soc.* **139**, 10055 (2017).
- [44] D. J. Kubicki, D. Prochowicz, A. Hofstetter, M. Sasaki, P. Yadav, D. Bi, N. Pellet, J. Lewiński, S. M. Zakeeruddin, M. Grätzel, and L. Emsley, Formation of stable mixed guanidinium-methylammonium phases with exceptionally long carrier lifetimes for high-efficiency lead iodide-based perovskite photovoltaics, *J. Am. Chem. Soc.* **140**, 3345 (2018).
- [45] A. A. Bakulin, O. Selig, H. J. Bakker, Y. L. Rezus, C. Müller, T. Glaser, R. Lovrincic, Z. Sun, Z. Chen, A. Walsh, J. M. Frost, and T. L. C. Jansen, Real-time observation of organic cation reorientation in methylammonium lead iodide perovskites, *J. Phys. Chem. Lett.* **6**, 3663 (2015).
- [46] A. M. A. Leguy, J. M. Frost, A. P. McMahon, V. G. Sakai, W. Kockelmann, C. Law, X. Li, F. Foglia, A. Walsh, B. C. O'Regan, J. Nelson, J. T. Cabral, and P. R. F. Barnes, The dynamics of methylammonium ions in hybrid organic-inorganic perovskite solar cells, *Nat. Commun.* **6**, 7124 (2015).
- [47] C. Motta, F. El-Mellouhi, S. Kais, N. Tabet, F. Alharbi, and S. Sanvito, Revealing the role of organic cations in hybrid halide perovskite $\text{CH}_3\text{NH}_3\text{PbI}_3$, *Nat. Commun.* **6**, 7026 (2015).
- [48] G. Liu, L. Kong, J. Gong, W. Yang, H. Mao, Q. Hu, Z. Liu, R. D. Schaller, D. Zhang, and T. Xu, Pressure-induced bandgap optimization in lead-based perovskites with prolonged carrier lifetime and ambient retainability, *Adv. Funct. Mater.* **27**, 1604208 (2017).
- [49] O. Selig, A. Sadhanala, C. Müller, R. Lovrincic, Z. Chen, Y. L. A. Rezus, J. M. Frost, T. L. C. Jansen, and A. A. Bakulin, Organic cation rotation and immobilization in pure and mixed methylammonium lead-halide perovskites, *J. Am. Chem. Soc.* **139**, 4068 (2017).
- [50] M. Kollár, L. Čirić, J. H. Dil, A. Weber, S. Muff, H. M. Ronnow, B. Náfrádi, B. P. Monnier, J. S. Luterbacher, L. Forró, and E. Horváth, Clean, cleaved surfaces of the photovoltaic perovskite, *Sci. Rep.* **7**, 695 (2017).
- [51] See Supplemental Material at <http://link.aps.org/supplemental/10.1103/PhysRevB.106.214106> for (i) waterfall plots of the temperature dependence of the real dielectric permittivity under pressure and (ii) additional analysis of two other vibration modes from our IR absorption spectra.
- [52] N. Onoda-Yamamuro, T. Matsuo, and H. Suga, Dielectric study of $\text{CH}_3\text{NH}_3\text{PbX}_3$ ($X = \text{Cl}, \text{Br}, \text{I}$), *J. Phys. Chem. Solids* **53**, 935 (1992).
- [53] G. Schuck, D. M. Töbrens, M. Koch-Müller, I. Efthimiopoulos, and S. Schorr, Infrared spectroscopic study of vibrational

- modes across the orthorhombic–tetragonal phase transition in methylammonium lead halide single crystals, *J. Phys. Chem. C* **122**, 5227 (2018).
- [54] N. Onoda-Yamamuro, T. Matsuo, and H. Suga, Calorimetric and IR spectroscopic studies of phase transitions in methylammonium trihalogenoplumbates (II), *J. Phys. Chem. Solids* **51**, 1383 (1990).
- [55] C. A. López, M. V. Martínez-Huerta, M. C. Alvarez-Galván, P. Kayser, P. Gant, A. Castellanos-Gomez, M. T. Fernández-Díaz, F. Fauth, and J. A. Alonso, Elucidating the methylammonium (MA) conformation in MAPbBr₃ perovskite with application in solar cells, *Inorg. Chem.* **56**, 14214 (2017).
- [56] *Broadband Dielectric Spectroscopy*, edited by F. Kremer and A. Schönhal, (Springer, Berlin, 2003).
- [57] J. Haruyama, K. Sodeyama, L. Han, and Y. Tateyama, First-principles study of ion diffusion in perovskite solar cell sensitizers, *J. Am. Chem. Soc.* **137**, 10048 (2015).
- [58] A. Senocrate, I. Moudrakovski, T. Acartürk, R. Merkle, G. Y. Kim, U. Starke, M. Grätzel, and J. Maier, Slow CH₃NH₃⁺ diffusion in CH₃NH₃PbI₃ under light measured by solid-state NMR and tracer diffusion, *J. Phys. Chem. C* **122**, 21803 (2018).
- [59] M. H. Futscher, J. M. Lee, L. McGovern, L. A. Muscarella, T. Wang, M. I. Haider, A. Fakharuddin, L. Schmidt-Mende, and B. Ehrler, Quantification of ion migration in CH₃NH₃PbI₃ perovskite solar cells by transient capacitance measurements, *Mater. Horiz.* **6**, 1497 (2019).
- [60] A. Poglitsch and D. Weber, Dynamic disorder in methylammoniumtrihalogenoplumbates (II) observed by millimeter-wave spectroscopy, *J. Chem. Phys.* **87**, 6373 (1987).
- [61] M. T. Weller, O. J. Weber, P. F. Henry, A. M. D. Pumpo, and T. C. Hansen, Complete structure and cation orientation in the perovskite photovoltaic methylammonium lead iodide between 100 and 352 K, *Chem. Commun.* **51**, 4180 (2015).
- [62] X. Lü, Y. Wang, C. C. Stoumpos, Q. Hu, X. Guo, H. Chen, L. Yang, J. S. Smith, W. Yang, Y. Zhao, H. Xu, M. G. Kanatzidis, and Q. Jia, Enhanced structural stability and photo responsiveness of CH₃NH₃SnI₃ perovskite via pressure-induced amorphization and recrystallization, *Adv. Mater.* **28**, 8663 (2016).
- [63] H. K. Mao, J. Xu, and P. M. Bell, Calibration of the ruby pressure gauge to 800 kbar under quasi-hydrostatic conditions, *J. Geophys. Res.* **91**, 4673 (1986).